Author version: *Geochem. Geophys. Geosyst., vol.13; 2012; Q10007, 11pp*

Tracing the Paleo sulfate-methane transition zones and H_2S seepage events in marine sediments: An application of C-S-Mo systematics

A.Peketi[1], A.Mazumdar[1]*, R.K. Joshi[1], D. J. Patil[2], P. L Srinivas[2], A.M. Dayal[2]

[1]*Geological Oceanography, National Institute of Oceanography, CSIR, Goa-403004, India*

[2]*National Geophysical Research Institute, Uppal Road, Hyderabad-500007, India*

**for correspondence: maninda@nio.org*

[1] Microbially mediated anaebic oxidation of methane (AOM) coupled with sulfate consumption within the sulfate methane transition zone (SMTZ) in marine sediments is a widely recorded biogeochemical reaction and has profound influence on the atmospheric CH_4 budget, marine carbon cycle and composition of sediment pore fluids. Recognising the paleo-SMTZs in the marine sediments/rock records can throw light on the variation of paleo-methane fluxes and occurrences of cold seep (H_2S+CH_4) events through geologic time. Here, we present results from carbonate carbon, pyrite sulfur and molybdenum analyses for two sediment cores overlying the methane hydrate deposits in the Bay of Bengal. The results show intimate association of isotopically depleted carbonate carbon and enriched pyrite sulfur, constraining the paleo SMTZ within the sediment column. In addition, anomalous enrichments of Mo concentrations indicate hydrogen sulfide seepage events. Here, we propose a geochemical tool using C-S-Mo sytematics to decipher the paleo-SMTZs in marine sediments and rocks.

Keywords: AOM, SMTZ, H_2S seepage, Molybdenum enrichment, sulfur isotope ratios.

1. Introduction

[2] SMTZ denotes a redox interface within the anoxic sediment column, where pore water sulfate and methane concentration profiles intersect and are depleted to non detectable concentrations. This depletion in sulfate and methane concentrations are attributed to the anaerobic oxidation of methane (AOM: Eq.1) performed by a syntrophic consortium of CH_4-oxidizing archaea and sulfate-reducing bacteria [*Reeburgh,* 2007*; Knittel and Boetius,* 2009].

$$CH_4 + SO_4^{2-} \rightarrow HCO_3^- + HS^- + H_2O \quad \text{(Eq. 1)}$$

The physical coupling of sulfate reducing bacteria and methanotrophs (ANME I, II) have been demonstrated by *Boetius et al.* [2000] and *Orphan et al.* [2001]. AOM prevents the release of methane into the atmosphere from ocean sediments, which would otherwise cause a major increase in green house gas concentrations. AOM consumes >90% of the total methane produced (85-300 Tg $year^{-1}$) in the oceanic sediments [*Hinrichs and Boetius,* 2002*; Reeburgh,* 2007]. Sulfate concentration profile and depth of SMTZ depend on the methane flux. High methane flux results in linear sulfate concentration gradient and shallow SMTZ and *vice versa* [*Borowski et al.,* 1996]. AOM causes marked enrichment in H_2S and HCO_3^- ion concentrations in the porewaters within SMTZ resulting in precipitation of Fe-sulfides (Eq. 2 and 3) and Ca-Mg-carbonates (Eq. 4) [*Berner,* 1970; *Jørgensen et al.,* 2004; *Ussler III and Paull,* 2008].

$$Fe^{2+} + HS^- \rightarrow FeS + H^+ \quad \text{(Eq. 2)}$$

$$FeS + S^o \rightarrow FeS_2 \quad \text{(Eq. 3)}$$

$$Ca^{2+} + HCO_3^- \rightarrow CaCO_3 + H^+ \quad \text{(Eq. 4)}$$

Dissolution and reprecipitation of barite across SMTZ have been reported by *Torres et al.,*1996; *Dickens,* 2001; *Synder et al.,* 2007 and *Solomon and Kastner*, 2011. In sulfate depleted pore waters, dissolution of barite leads to enhanced pore water Ba^{2+} concentrations. Upward mobilzation of Ba^{2+} exceeding the barite burial and downward diffusive flux of SO_4^{2-} results in the development of barite front just above the SMTZ [*Dickens*, 2001].

[3] In this work, we have aimed at the development of a geochemical tool using C-S-Mo sytematics to identify paleo-SMTZs and H_2S seepage events in marine sedimentary deposits. We have carried out this investigation in two closely spaced cores (less than 105.2 m apart) of lengths 30 m (**MD161-8**: *Lat.:*15^0*51.8624N, Long.:* 81^0*50.0692E*) and 198 m (**NGHP-01-**

10D:*Lat.:15^{0}51.8609N, Long.:81^{0}50.0749E,*) from a water depth of ~1030 m off Krishna-Godavari (K-G) basin, East coast of India (Fig. 1).

2. Geology

[4] Krishna-Godavari basin (K-G basin) is a pericratonic rift basin located in the eastern continental margin of India (ECMI), covering an area of 28,000 km^2 onshore and 145,000 km^2 offshore [*Rao,* 2001]. The ECMI represents a passive continental margin and evolved through the break-up of eastern Gondwana landmass 130 Ma ago when India separated from East Antarctica [*Ramana et al.,* 2001]. Andhra alluvium and Godavari clay comprise the onshore and offshore deposits of Holocene-Pleistocene epochs. Offshore sedimentation took place under oxic bottom water condition. The widespread occurrence of Bottom Simulating Reflector (BSR) in the seismic data [*Dewangan et al.,* 2010] and drilling/ logging activities onboard JOIDES *Resolution* suggest the presence of gas hydrate (30 to 150 mbsf) in K-G basin [*Collett et al.,* 2008]. BSR is believed to appear due to the acoustic impedance contrast between the overlying gas hydrate deposit and the underlying free gas layer. *Dewangan et al.* [2010] reported various structures formed due to shale tectonism/neotectonism such as bathymetric mounds, deep-seated shale diapirs and toe thrust faults from the K-G basin. These bathymetric mounds are commonly associated with fluid/gas migration features and show numerous fault/fracture systems which facilitate the accumulation of gas hydrate and focussed fluid flow [*Dewangan, et al.,* 2010]. BSR-derived geothermal gradient (GTG) in the vicinity of the study site NGHP-01-10D [*Dewangan, et al.,* 2011] shows an abnormal increase in GTG from a background value of 38^{o}C/km to ~45^{o}C/km at the top of the mound which is primarily related to fluid advection along the fault system.

3. Methodology

[5] The sediment cores MD161-8 and NGHP-01-10D were collected on board Marian Dufresne and JOIDES-Resolution respectively. For the solid phase analyses NGHP-01-10D was sub-sampled at intervals of 1.5 to 6 m following ODP sampling protocol, whereas, MD161-8 was sub-sampled at 20 to 50 cm intervals. Samples were packed in nitrogen filled heat sealed plastic bags to avoid sulfide oxidation by atmospheric oxygen and stored at 4^{o}C. Carbon and oxygen isotope ratios of carbonate in bulk sediments and mineral separates were determined with a Thermo Delta V continuous flow isotope ratio mass spectrometer coupled with a GASBENCH II equipped with a PAL autosampler. The carbon isotope and oxygen results are reported in standard delta notation as permil deviation from the VPDB standard. A sample reproducibility of 0.1‰ for both carbon and

oxygen is reported here. Total Inorganic carbon (TIC) content was determined by carbon coulometer (UIC–CM5130). Total carbon (TC) content was measured by elemental analyzer (Thermo CNS 2500). Total organic carbon (TOC) was calculated by subtracting TIC from TC. Reproducibility for TIC and TC are 0.1 %.

[6] Elemental sulfur was extracted from an aliquot of homogenized wet sample by shaking it with dichloromethane on a vortex shaker for 2 hours. Dichloromethane was removed by centrifugation. Acid volatile sulfur (AVS) and Chromium reducible sulfur (CRS) were extracted from the S^0 free sediments following a two step extraction procedure using 6N HCl and 1M $CrCl_2$ sequentially in an oxygen free reaction vessel with continuous nitrogen flow. H_2S produced by reduction of sulfide was trapped as ZnS in zinc acetate solution (pH>11) and subsequently reprecipitated as Ag_2S by adding $AgNO_3$ [*Canfield et al.,* 1986]. Sulfur stable isotope ratio measurement of the pure Ag_2S precipitates was carried out with a Thermo Delta V Plus continuous flow isotope ratio mass spectrometer coupled to an elemental analyzer (EA 1112). All results are reported in the standard delta notation as permil deviations from the VCDT (Vienna Canyon Diablo Troilite). Sample reproducibility better than 0.3‰ is reported here. Mo and Ba concentrations were measured following Li-metaborate/tetraborate fusion method at Actalabs, Canada. Fused samples were dissolved in nitric acid and concentrations were measured using an ICP-MS. Reproducibilities for Mo and Ba concentrations are better than 1 and 3 ppm respectively. Al concentration in desalinated sediment samples was determined by X-ray Fluorescence (PANalytical Axios) technique using fused pellets. Reproducibility for Al is better than 3 wt %. Mineralogical identification was carried out using a Rigaku X-ray diffractometer (Ultima-IV). All the carbonate samples were run from 25 to 32° 2θ at 1°/min scan speed using CuK_α radiation (λ = 1.541838Å). The Mg (mole%) is calculated [*Joshi et al.,* in prep.] using a Mg (mole %) - d-spacing standard curve in *Hardy and Tucker* [1988].

4. Results

[7] The analytical results are presented in table-1 and 2. At MD161-8, CRS concentrations vary from 0.04 to 3.7 wt % (Fig. 2A). $\delta^{34}S_{CRS}$ varies from -44.4 to +21‰ (Fig. 2 B). Upwards from 18 mbsf, $\delta^{34}S_{CRS}$ shows a decrease from enriched to depleted isotope ratios. TIC contents range from 0.1 to 2 wt % and show several high concentration peaks throughout the core (Fig. 2 C). Total organic content (TOC) varies from 1 to 2.1 wt % (Table 1). $\delta^{13}C_{TIC}$ varies from -43. to -1.1 ‰ (Fig. 2 D). A most pronounced carbon isotope depletion is recorded within 8.32-11.05 mbsf and 17.05-30 mbsf. $\delta^{18}O_{TIC}$ values vary from -3.4 to +3.9‰ (Fig. 2D). A negative correlation is apparent between

the profiles of carbon and oxygen isotope ratios. Ba/Al ratio varies from 0.002-0.003 (Fig. 2 E). Mo content varies from <2 to 37 ppm (Fig. 2 B). Mg mole % in the picked carbonate varies from 2.8 to 19.4 % [*Joshi et al.*, in prep.]. The age scale for MD161-8 is based on ^{14}C dates [*Mazumdar et al.* 2009].

[8] At NGHP-01-10D, CRS content ranges from 0.01 to 1.7 wt% (Fig. 3A). $\delta^{34}S_{CRS}$ varies from -43.8 to +24‰ and shows repeated fluctuations between depleted and enriched isotope ratios (Fig. 3B). TIC content ranges from 0.2-2 wt % (Fig. 3C) and total organic content (TOC) varies between 0.5 to 2.1 wt% (Table-2). $\delta^{13}C_{TIC}$ varies from -43.9 to +6.5‰ (Fig. 3D). The most depleted carbon isotope ratios are recorded at 19.5 and 43.7 mbsf, whereas, below 45.7 m, $\delta^{13}C_{TIC}$ values are close to 0 ‰ or moderately enriched (up to 6.5 ‰). The carbonate grain separates also show enriched carbon isotope ratios (-0.68 to +12.8 ‰) in deeply buried layers (Fig. 3 D). $\delta^{18}O_{TIC}$ varies from -2.3 to +3.6 ‰ (Fig. 3 D). A negative correlation is apparent between the profiles of carbon and oxygen isotope ratios within 45 mbsf. Ba/Al ratio ranges from 0.0017 to 0.0031(Fig. 3E). Mo content varies from <2 to 13 ppm (Figure 3B).

5. Discussion

5.1 $\delta^{13}C_{TIC}$: Signature of AOM

[9] Sulfate consumption and alkalinity production in sediment porewaters via AOM and organo-clastic degradation can be represented by equations 1 and 5 respectively.

$$SO_4^{2-} + 2CH_2O \rightarrow H_2S + 2HCO^-_3 \qquad \text{(Eq. 5)}$$

Contrary to organo-clastic oxidation (Eq. 5), AOM results in the depth-focussed sulfate consumption and bicarbonate production at the SMTZ leading to precipitation of Ca-Mg carbonates (Eq. 4) with depleted carbon isotopic ratios [*Ussler III and Paul, 2008*]. Occurrences of high Mg-calcite (HMC) with highly depleted carbon isotope ratios (Figs. 2D, 3D and 4) indicate intensification of AOM [*Aloisi et al.,* 2000; *Greinert et al.,*2001; *Nöthen and Kasten,* 2011]. HMC precipitation is favoured under low sulfate conditions. HMC and dolomites have been shown to dominantly precipitate within or below the SMTZ [*Greinert et al.*, 2001]. $\delta^{13}C_{CH4}$ values (-60 to -85.5‰) suggest a possible biogenic origin of methane at the studied location [*Mazumdar et al.,* 2009]. The $\delta^{13}C_{TIC}$ reported here is partially influenced by the presence of foraminifera with the calcareous test having $\delta^{13}C$ value ranging from -1 to +1‰ [*Joshi and Mazumdar,* 2011; *Joshi et al.,* in prep.]. High TIC contents

(Figure 2C and 3C) corresponding in depth to the depleted carbon isotope ratios suggest the accumulation of authigenic carbonate in the sediment. Enriched oxygen isotope ratios corresponding to depleted carbon isotope ratios (Figure 2D and 3D) possibly indicate modification of pore water oxygen isotope ratios due to thawing of methane hydrate [*Greinert et al.,*2001]. The $\delta^{13}C_{TIC}$ in NGHP-01-10D does not show depletion below 50m due to burial diagenesis or precipitation of carbonate from isotopically enriched bicarbonate pool [*Moore et al.,*2004]. Enrichement in carbon isotope ratios were also recorded in hand-picked isolated authigenic carbonate grains (Fig. 3D (green traingles) and Fig. 4). Relative enrichment of ^{13}C in residual pore water CO_2 with depth is commonly attributed to the production of isotopically depleted methane via the CO_2 reduction pathway [*Whiticar,* 1999].

5.2 Mo anomaly: Evidence of Hydrogen sulfide seepage

[10] Molybdenum behaves conservatively in oxic seawater and has a residence time ranging from 440 to 780 ka [*Emerson and Huested,* 1991; *Miller et al.,*2011]. Under oxic marine bottom water conditions, Mo exists as $Mo(VI)O_4^{2-}$ (molybdate). However, under sulfidic bottom water conditions, Mo is eventually scavenged as tetrathiomolybdate ($Mo(IV)S_4^{2-}$) from sea water by FeS [*Helz et al., 2004*] (Eq.6 and 7).

$$MoO_4^{2-} + 4H_2S \rightarrow MoS_4^{2-} + 4H_2O \qquad \text{(Eq. 6)}$$

$$Fe^{2+} + H_2S + 2OH^- \rightarrow FeS + 2H_2O \qquad \text{(Eq. 7)}$$

Experimental results show that the coprecipitation of ($Mo(IV)S_4^{2-}$) with FeS occurs above a threshold concentration of ~11µM H_2S (at 298K, 1atm) [*Erikson and Helz,* 2000]. The redox transformation of Mo and its anomalous enrichment in marine sediments is an established proxy for paleo sulfidic bottom water conditions [*Emerson and Huested,* 1991*; Crusius et al.,* 1996; *Lyons et al.,* 2003; *Helz et al.,* 2004]. On the other hand, *Helz et al.*, [2011] emphasized the importance of pH in molybdenum removal in euxinic basins. Although FeS is the primary scavenger of Mo from sulfidic bottom waters, it is eventually hosted by pyrite and organic matter in marine sediments [*Helz et al.,*2004; *Tribovillard et al.,* 2004]. Mo concentration profiles of MD161-8 and NGHP-01-10D show marked anomalies within the top 50 mbsf relative to back ground Mo concentration (<2 ppm) in the sediment which is close to the crustal average (~1 ppm) [*Taylor and Mcheannam,* 1985]. The Mo enrichment peaks suggest at least three events of H_2S build up at or above the sediment water interface, attributed to H_2S seepage (Figure 2B and 3B). Further investigation is required on the

possibility of Mo contribution from degradation of labile organic matter and mineral phases with the absorbed Mo [*Siebert et al.,* 2006]. H_2S enrichment and seepage is attributed to intense AOM (Eq.2) close to the sediment water interface. The apparent occurrences of H_2S seepages at our studied sites is also supported by the presence of chemosynthetic clams like *Callyptogena sp., Vesicomaya sp., Lucinoma sp.* and chemical signatures of archaeal mat within 16-18 mbsf at MD161-8 and NGHP-01-10D [*Collett et al.,*2008; *Mazumdar et al.* 2009, 2011a]. The archaeal mat is identified on the basis of archaeal lipid compound 2, 6, 10, 15, 19-pentamethyicosane (PMI) with extreme depletion in ^{13}C ($\delta^{13}C_{PMI}$ -106 to -139 ‰ : *Joshi and Mazumdar,* 2011; *Mazumdar et al.,*2011b).

5.3 $\delta^{34}S_{CRS}$: Signature of Paleo-SMTZ

[11] CRS concentration profiles (Figure2 A, 3 A) essentially represent the pyritization trend through the sediment column. CRS concentrations depend on the availability of reactive iron during early/late diagenetic stages and hydrogen sulfide concentrations in the sediments [*Neuman et al.,*2005]. Since pyritization involves insignificant sulfur isotope fractionation, pyrite isotope ratios represent the sulfur isotope ratio of pore water HS^- [*Price and Shieh,* 1979]. Hence, signature of AOM induced sulfate reduction process at the SMTZ may be archived as $\delta^{34}S_{CRS}$. Highly depleted sulfur isotope ratios (-31.8 to -44.4 ‰) of CRS recorded in our study (Figure 2 B and 3 B) suggest disproportionation of sulfur intermediates like S^0, SO_3^{2-} and $S_2O_3^{2-}$ produced during oxidative part of sulfur cycle [*Canfield and Thamdrup,* 1994]. Disproportionation may play an important role in early diagenetic sulfidization close to the sediment water interface due to high burrowing activities leading to the oxidation of HS^- [*Canfield and Farquhar,* 2009]. However, field observations [*Wortmann et al.,* 2001], experimental [*Sim et al.,* 2011] and modelling (*Brunner and Bernasconi*, 2005) studies suggest significant depletion in ^{34}S and fractionation up to 70‰ may be directly caused by dissimilatory sulfate reduction without disproportionation of sulfur intermediates. The depth zone from 19 to 30 mbsf in MD161-8 shows marked enrichment in ^{34}S in two successive stages (I and II). The rise in $^{34}S_{CRS}$ is attributed to build-up of isotopically enriched HS^- pool via AOM (Eq. 2) fuelled by an enhanced vertical methane flux [*Borowski et al.,*1996]. The enrichment of ^{34}S in the residual pore water sulfate (source of H_2S) is caused by higher rate of sulfate reduction than the rate of sulfate diffusion into the sediment pore volume from overlying seawater [*Jørgensen,* 1979]. $\delta^{34}S_{CRS}$ values up to +21‰ (Figure 2B) suggest the near quantitative consumption of pore water sulfate having sea water like sulfur isotope ratio in a closed system because of intensification in methane flux [*Kaplan and Rittenberg,* 1964; *Wehrmann et al.,* 2011]. Intensification of AOM is also supported by the occurrence of isotopically depleted authigenic carbonates within this zone (Figure 2D). An enhanced

methane flux at or across the sediment water interface resulted in the H_2S seepage as indicated by the Mo anomaly within 14 to 19 mbsf. The steady decline in $\delta^{34}S_{CRS}$ values within this zone suggests a major contribution of isotopically depleted H_2S derived from near surface sulfate reduction (open system: *Jørgensen*, 1979] relative to the flux of isotopically enriched H_2S generated by AOM occurring deeper in the subsurface [*Jørgensen et al.,* 2004; *Wehrmann et al.,* 2011]. The drop in Mo concentration indicates a diminished H_2S seepage likely due to a weakening of AOM activity. A sharp $\delta^{34}S_{CRS}$ peak superimposed on the steady decline within the interval 14 to 19 mbsf possibly represents recent pyritization at the present SMTZ located at 15-16 mbsf [*Mazumdar et al.,* 2009]. A second seepage event recorded within 8-14 mbsf suggests re-intensification of AOM. The net $\delta^{34}S_{CRS}$ values recorded in this zone is attributed to the dominance of an isotopically depleted H_2S pool produced via organoclastic/disproportionation pathways. Thus $\delta^{34}S_{CRS}$ coupled with carbon isotope ratios of bulk inorganic carbon ($\delta^{13}C_{TIC}$) can be used to trace paleo intensification of AOM.

[12] In NGHP-01-10D, the repeated occurrence of zones of isotopically enriched CRS indicates the episodic intensification of AOM due to enhanced vertical methane flux. Within the top 50 mbsf, high $\delta^{34}S_{CRS}$ coupled with low $\delta^{13}C_{TIC}$ values indicate an AOM derived HS^- and bicarbonate pool. However, the down depth enrichment of ^{13}C in TIC of the deeper sediments is attributed to overprinting by late diagenetic carbonate precipitation. Two broad Mo concentration anomalies are observed in this core. The Mo anomaly at ~40 mbsf is the oldest H_2S seepage event observed in this study. High resolution sampling and analyses is required for better understanding of C-S-Mo systematics in NGHP-01-10D.

5.4 Absence of barium front

[13] The Ba/Al ratios (Fig. 2 E and 3 E) do not show any sharp peak typical of barium fronts in the sediment column [*Torres et al.,* 1996; *Gingele et al.,* 1999; *Snyder et al.,* 2007]. Barium fronts develop just above the sulfate methane interface due to precipitation of $BaSO_4$ which is controlled by the upward flux of Ba^{2+} from sulfate depleted to sulfate enriched zone across the sulfate-methane interface [*Dickens,* 2001]. A Ba front has traditionally been interpreted as an indicator of paleo-SMTZ [*Dickens,* 2001; *Riedinger et al.,* 2006]. The absence of Ba/Al enrichment peak in the studied cores indicates possible dissolution of barite due to upward movement of SMTZ, or a low productivity linked Ba flux to the sediment. Hence, in our study the Ba/Al ratio is inconclusive in defining paleo-SMTZs.

5.5 Intensification of AOM: methane source

[14] The episodic intensification of AOM as indicated in our study can be linked to the waxing and waning of the methane flux through the sediment column. Enhanced methane flux may be linked to hydrate destabilization, triggered by tectonism and/or fluctuation in ocean bottom pressure-temperature conditions [*Carson and Screaton,*1998*; Dickens,* 2003; *Max et al.,* 2008]. At our studied location, the high geothermal gradient and shale tectonics related diapiric mound and fault system indicate a possible influence of passive tectonism on hydrate stability [*Dewangan et al*., 2011].

6. Conclusions

[15] In this study we propose C-S-Mo systematics in marine sediments as a potential tool, to identify paleo-SMTZs and sulfide seepage events. This approach is especially useful in the absence of a well defined barite front traditionally considered as a SMTZ indicator. We have observed the intimate association of isotopically enriched pyrite sulfur and strongly depleted ($\delta^{13}C$) high magnesian calcite in the sediment column. Extreme AOM at or above sediment water interface results in the seepage of hydrogen sulfide leading to Mo enrichment in sediment due to co-precipitation of Mo and Fe-monosulfides.

[16] **Acknowledgements.** We thank the directors of NIO, NIOT, NCAOR, advisor MOES, NGHP (India) for supporting this study. Head oceanography department and in-charge on-board operations of IPEV are thanked for providing onboard technical support and facilities. Sincere thanks to students of Goa University, IIT Kharagpur and project scientists of NIO, NIOT, PRL and NGRI. Thanks are due to M. Caesar for carrying out XRF analyses at NIO. Research fellowship from VNJCT to A.Peketi is sincerely acknowledged. We are grateful for the comments and suggestions provided by Dr. Tatania Goldberg and by an anonymous reviewer which significantly improved the manuscript.

References

Aloisi, G., C. Pierre, J. M. Rouchy, J. P. Foucher, and J. Woodside (2000), Methane-related authigenic carbonates of eastern Mediterranean Sea mud volcanoes and their possible relation to gas hydrate destabilisation, *Earth Planet. Sci. Lett., 184,* 321-338, doi:10.1016/S0012-821X(00)00322-8.

Berner, R. (1970), Sedimentary pyrite formation, *American J. Sci. 268*, 1-23.

Boetius, A., K. Ravenschlag, C. J. Schubert, D. Rickert, F. Widdel, A. Giesecke, R. Amann, B. B. Jørgensen, U. Witte, and O. Pfannkuche (2000), A marine microbial consortium apparently mediating anaerobic oxidation of methane, *Nature*, *407*, 623-626, doi:10.1038/35036572.

Borowski, W., C. Paull, and W. Ussler III (1996), Marine pore-water sulfate profiles indicate in situ methane flux from underlying gas hydrate, *Geology*, *24*, 655-658, doi: 10.1130/0091-7613.

Brunner, B., and S. M. Bernasconi (2005), A revised isotope fractionation model for dissimilatory sulfate reduction in sulfate reducing bacteria, *Geochim. Cosmochim, 69*, 4773–4785, doi: 10.1016/j.gca.2005.04.017.

Canfield, D., R. Raiswell, J. Westrich, M .Christopher, C. M., Reaves, and R. A. Berner (1986), The use of chromium reduction in the analysis of reduced inorganic sulphur in sediments and shales, *Chem. Geol.*, *54*, 149-155.

Canfield, D., and B. Thamdrup (1994), The production of ^{34}S-depleted sulfide during bacterial disproportionation of elemental sulfur, *Science*, *266*, 1973-1975, doi:10.1126/science.11540246.

Canfield, D. E., and J. Farquhar (2009), Animal evolution, bioturbation, and the sulfate concentration of the oceans, *PNAS*, *106*, 8123-8127, doi:10.1073/pnas.0903380106.

Carson, B., and E. J. Screaton (1998), Fluid flow in accretionary prisms: Evidence for focused, time-variable discharge, *Rev. Geophys., 36*, 329-351, doi:10.1029/97RG03633.

Collett, T., M. Riedel, J. Cochran, R. Boswell, J. Presley, P. Kumar, A. Sathe, A. Sethi, M. Lall, and V. Sibal (2008), The NGHP Expedition 01 Scientists, Indian National Gas Hydrate Program Expedition 01 Initial Reports.

Crusius, J., S. Calvert, T. Pedersen, and D. Sage (1996), Rhenium and molybdenum enrichments in sediments as indicators of oxic, suboxic and sulfidic conditions of deposition, *Earth Planet. Sci. Lett., 145*, 65-78, doi:10.1016/S0012-821X(96)00204-X.

Dewangan, P., T. Ramprasad, M. Ramana, A. Mazumdar, M. Desa, and F. Badesab (2010), Seabed Morphology and Gas Venting Features in the Continental Slope Region of Krishna-Godavari Basin, Bay of Bengal: Implications in Gas-Hydrate Exploration, *Mar. and Petrol. Geol., 27*, 1628-1641, doi:10.1016/j.marpetgeo.2010.03.015.

Dewangan, P., G. Sriram, T. Ramprasad, M. V. Ramana, and P. Jaiswal (2011), Fault system and thermal regime in the vicinity of site NGHP-01-10, Krishna-Godavari basin, Bay of Bengal, *Mar. and Petrol. Geol. 28*, 1899-1914, doi:10.1016/j.marpetgeo.2011.03.009.

Dickens, G. R. (2001), Sulfate profiles and barium fronts in sediment on the Blake Ridge: Present and past methane fluxes through a large gas hydrate reservoir, *Geochim. Cosmochim. Acta, 65*, 529-543.

Dickens, G. R. (2003), Rethinking the global carbon cycle with a large, dynamic and microbially mediated gas hydrate capacitor, *Earth Planet. Sci. Lett.*, *213*, 169-183, doi:10.1016/S0012-821X(03)00325-X.

Emerson, S. R., and S. S. Huested (1991), Ocean anoxia and the concentrations of molybdenum and vanadium in seawater, *Mar. Chem., 34*, 177-196, doi:10.1016/0304-4203(91)90002-E.

Erickson, B. E., and G. R. Helz (2000), Molybdenum (VI) speciation in sulfidic waters: Stability and lability of thiomolybdates, *Geochim. Cosmochim. Acta*, *64,* 1149-1158, doi: 10.1016/S0016-7037(99)00423-8.

Gingele, F. X., M. Zabel, S. Kasten, W. J. Bonn, and C. C. Nürnberg (1999), Biogenic Barium as a proxy for paleoproductivity: methods and limitations of Application, *Use of proxies in paleoceanography: examples from South Atlantic,* vol. 164, edited by, Fisher, G. and G. Wefer, Springer-Verlag, Berlin, pp. 345-364.

Greinert, J., G. Bohrmann, and E. Suess (2001), Gas hydrate-associated carbonate and methane-venting at Hydrate Ridge: classification, distribution and origin of authigenic lithologies, in *Natural gas hydrate: occurrence, distribution and detection, Geophysical Monograph,* vol. 124, edited by, C. K. Paul & W. P Dillon, pp. 99-113.

Hardy, R and M. Tucker (1988), X-ray powder diffraction of sediments, in *Techniques in Sedimentlogy*, edited by, M. Tucker, pp 191-228, Blackwell Scientific Publication, Oxford.

Helz, G. R., T. P. Vorlicek, and M. D. Kahn (2004), Molybdenum scavenging by iron monosulfide, *Environ. Sci. & Tech., 38*, 4263-4268, doi: 10.1021/es034969+.

Helz, G. R., E. B. Nakić, N. Mikac, and I. Ciglenečki (2011), New model for molybdenum behavior in euxinic waters, *Chem. Geo., 284*, 323–332, doi:10.1016 /j.chemgeo.2011.03.012.

Hinrichs, K. U., and A. B. Boetius (2002), The anaerobic oxidation of methane: new insights in microbial ecology and biogeochemistry, in *Ocean Margin Systems*, edited by G. D. Wefer, et al., pp. 457-477, Springer-Verlag, Heidelberg.

Jørgensen, B. (1979), A theoretical model of the stable sulfur isotope distribution in marine sediments, *Geochim. Cosmochim. Acta*, *43*, 363-374.

Jørgensen, B., M. Böttcher, H. Lüschen, L. Neretin, and I. Volkov (2004), Anaerobic methane oxidation and a deep H_2S sink generate isotopically heavy sulfides in Black Sea sediments, *Geochim. Cosmochim. Acta, 68*, 2095-2118, doi:10.1016/j.gca.2003.07.017.

Joshi, R. K., and A. Mazumdar (2011), Hydrate Destabilization and Methane Release Events during Last Glacial Episode in Bay of Bengal, Goldschmidt Conference, Prague, Abstract, 1127.

Kaplan, I., and S. Rittenberg (1964), Microbial fractionation of sulfur isotopes, *J. Gen. Microbiol., 34*, 195-212.

Knittel, K., and A. Boetius (2009), Anaerobic oxidation of methane: progress with an unknown process, *Annu. Rev. Micro., 63*, 311-334, doi: 10.1146/annurev.micro.61.080706.093130.

Lyons, T. W., J. P. Werne, D. V. Hollander, and R. W. Murray (2003), Contrasting sulfur geochemistry and Fe/Al and Mo/Al ratios across the last oxic-to-anoxic transition in the Cariaco Basin, Venezuela, *Chem. Geol. 195,* 131-157, doi:10.1016/S0009-2541(02)00392-3.

Max, M. D., A. H. Johnson, and W. P. Dillon (2008), Economic geology of natural gas hydrates, Dordrecht, Netherlands, Springer publishers, 341p.

Mazumdar, A., P. Dewangan, H. Joäo, A. Peketi, V. Khosla, M. Kocherla, F. Badesab, R. Joshi, P. Roxanne, and P. Ramamurty (2009), Evidence of paleo–cold seep activity from the Bay of Bengal, offshore India, *Geochem. Geophys. Geosyst., 10*, Q06005. doi:10.1029/2008GC002337.

Mazumdar, A., R. K. Joshi, A. Peketi, and M. Kocherla (2011a), Occurrence of faecal pellet-filled simple and composite burrows in cold seep carbonates: A glimpse of a complex benthic ecosystem, *Mar. Geol.*, *289*, 117-121, doi:10.1016/j.margeo.2011.09.003.

Mazumdar A, R. K. Joshi, A. Peketi, and B. G. Naik (2011b), Variation in carbon stable isotope ratios of organic matter in Bay of Bengal during the last glacial Episode, Goldschmidt conference, Prague, Abstracts, p.1435.

Miller, C. A., B. Peucker-Ehrenbrink, B. D. Walker and F. Marcantonio (2011), Re-assessing the surface cycling of molybdenum and rhenium, *Geochim. Cosmochim. Acta,75*, 7146-7179, doi:10.1016/j.gca.2011.09.005.

Moore, T. S., R. W. Murray, A. C. Kurtz, and D. P. Schrag (2004), Anaerobic methane oxidation and the formation of dolomite, *Earth Planet. Sci. Lett.*, *229*, 141-154, doi:10.1016/j.epsl.2004.10.015.

Neumann, T., N. Rausch, T. Leipe, O. Dellwig, Z. Berner, M. Böttcher, and E. Michael (2005), Intense pyrite formation under low-sulfate conditions in the Achterwasser lagoon, SW Baltic Sea, *Geochim. Cosmochim. Acta, 69*, 3619-3630, doi: 10.1016/j.gca.2005.02.034.

Nöthen, K., and S. Kasten (2011), Reconstructing changes in seep activity by means of pore water and solid phase Sr/Ca and Mg/Ca ratios in pockmark sediments of the Northern Congo fan, *Mar. Geol., 287,* 1-13, doi:10.1016/j.margeo.2011.06.008.

Orphan, V. J., C. H. House, K. U. Hinrichs, K. D. McKeegan, and E. F. DeLong (2001), Methane-consuming archaea revealed by directly coupled isotopic and phylogenetic analysis, *Science*, *293*, 484 - 487, doi: 10.1126/science.1061338.

Price, F., and Y. Shieh (1979), Fractionation of sulfur isotopes during laboratory synthesis of pyrite at low temperatures, *Chem. Geol., 27*, 245-253.

Ramana, M. V., K. S. Krishna, T. Ramprasad, M. Desa, V. Subrahmanyam, and K. V. L. N. S. Sarma (2001), Structure and tectonic evolution of the northeastern Indian Ocean, in: *The Indian Ocean: A Perspective,* edited by Sen Gupta, R., and E. Desa, pp. 731-816, Oxford & IBH, New Delhi (India).

Rao, G., (2001), Sedimentation, stratigraphy, and petroleum potential of Krishna-Godavari basin, East Coast of India, *AAPG bulletin, 85*, 1623-1643.

Reeburgh, W. S. (2007), Oceanic methane biogeochemistry, *Chem. Rev., 107*, 486-513, doi: 10.1002/chin.200720267.

Riedinger, N., S. Kasten, J. Gröger, C. Franke, and K. Pfeifer (2006), Active and buried authigenic barite fronts in sediments from the Eastern Cape Basin, *Earth Planet. Sci. Lett., 241,* 876-887, doi:10.1016/j.epsl.2005.10.032.

Sim, M. S., T. Bosak, and S. Ono (2011). Large sulfur isotope fractionation does not require disproportionation, *Science 333*, 74-77, doi: 10.1126/science.1205103.

Siebert, C., J. M. Manus, A. Bice, R. Poulson, and W. M. Berelson (2006), Molybdenum isotope signatures in continental margin marine sediments, *Earth Planet. Sci. Lett.,* 241, 723 – 733, doi:10.1016/j.epsl.2005.11.010.

Solomon, E. A., and M. Kastner (2011), Progressive barite dissolution in the Costa Rica forearc – Implications for global fluxes of Ba to the volcanic arc and mantle, *Geochim. Cosmochim. Acta 83*, 110–124, doi:10.1016/j.gca.2011.12.021.

Snyder, G. T., G. R. Dickens, and D. G. Castellini (2007), Labile barite contents and dissolved barium concentrations on Blake Ridge: New perspectives on barium cycling above gas hydrate system, *Jour. Geochem. Expl., 95,* 48-65, doi:10.1016/j.gexplo.2007.06.001.

Taylor, S. R., and S. M. McLennan, (1985), The Continental Crust: its Composition and Evolution, pp.312, Blackwell, Oxford.

Torres, M. E., H. J. Brumsack, G. Bohrmann, and K. C. Emeis (1996), Barite fronts in continental margin sediments: A new look at barium remobilization in the zone of sulfate reduction and formation of heavy barites in diagenetic fronts, *Chem. Geol., 127,* 125-139.

Tribovillard, N., A. Riboulleau, T. Lyons, and F. Baudin (2004), Enhanced trapping of molybdenum by sulfurized marine organic matter of marine origin in Mesozoic limestones and shales, *Chem. Geol., 213,* 385– 401, doi:10.1016/j.chemgeo.2004.08.011.

Ussler III, W., and C. K. Paull (2008), Rates of anaerobic oxidation of methane and authigenic carbonate mineralization in methane-rich deep-sea sediments inferred from models and geochemical profiles, *Earth Planet. Sci. Lett.*, *266*, 271-287, doi:10.1016/j.epsl.2007.10.056.

Wehrmann, L. M., S. P. Templer, B. Brunner, M. Stefano, S. M. Bernasconi, L. Maignien, and T. G. Ferdelman (2011), The imprint of methane seepage on the geochemical record and early diagenetic processes in cold-water coral mounds on Pen Duick Escarpment, Gulf of Cadiz, *Mar. Geol., 282*, 118–137, doi:10.1016/j.margeo.2010.08.005.

Whiticar, M. J. (1999), Carbon and hydrogen isotope systematics of bacterial formation and oxidation of methane, *Chem. Geol., 161,* 291–314.

Wortmann, U. G., S. M. Bernasconi, and M. E. Böttcher (2001), Hypersulfidic deep biosphere indicates extreme sulfur isotope fractionation during single-step microbial sulfate reduction, *Geology, 29*, 647–650, doi:10.1130/0091-7613(2001)029<0647: HDBIES>2.0.CO;2.

Captions:

Figure 1: Map showing coring locations of MD161-8 and NGHP-01-10D off Krishna Godavari basin, Bay of Bengal, India.

Figure 2. Vertical profiles of concentrations and isotope ratios of core MD161-8. **A:** CRS (wt%), **B:** Mo (ppm) and $\delta^{34}S_{CRS}$ (VCDT ‰). Dotted line indicate $\delta^{34}S$ value of sea water sulfate, **C:** TIC (wt%), **D:** $\delta^{13}C_{TIC}$ and $\delta^{18}O_{TIC}$ (VPDB ‰), **E:** (Ba/Al)*10^3. The calibrated ^{14}C ages (ky BP) are from *Mazumdar et al.* [2009].

Figure 3. Vertical profiles of concentrations and isotope ratios of core NGHP-01-10D. **A:** CRS (wt%), **B:** Mo (ppm) and $\delta^{34}S_{CRS}$ (VCDT ‰). Blue arrows indicate zones of sulfur isotope enrichment. Dotted line indicate $\delta^{34}S$ value of sea water sulfate, **C:** TIC (wt%), **D:** $\delta^{13}C_{TIC}$ and $\delta^{18}O_{TIC}$ (VPDB ‰). Green triangles indicate carbon isotope ratios of handpicked authigenic carbonate grains, **E:** (Ba/Al)*10^3.

Figure 4. Mg content (mol%) and carbon isotope ratios of handpicked authigenic carbonates from the core MD161-8 [*Joshi et al*., in prep.].

Table 1. Elemental concentrations and isotopic ratios of MS161-8.

Table 2. Elemental concentrations and isotopic ratios of NGHP-01-10D.

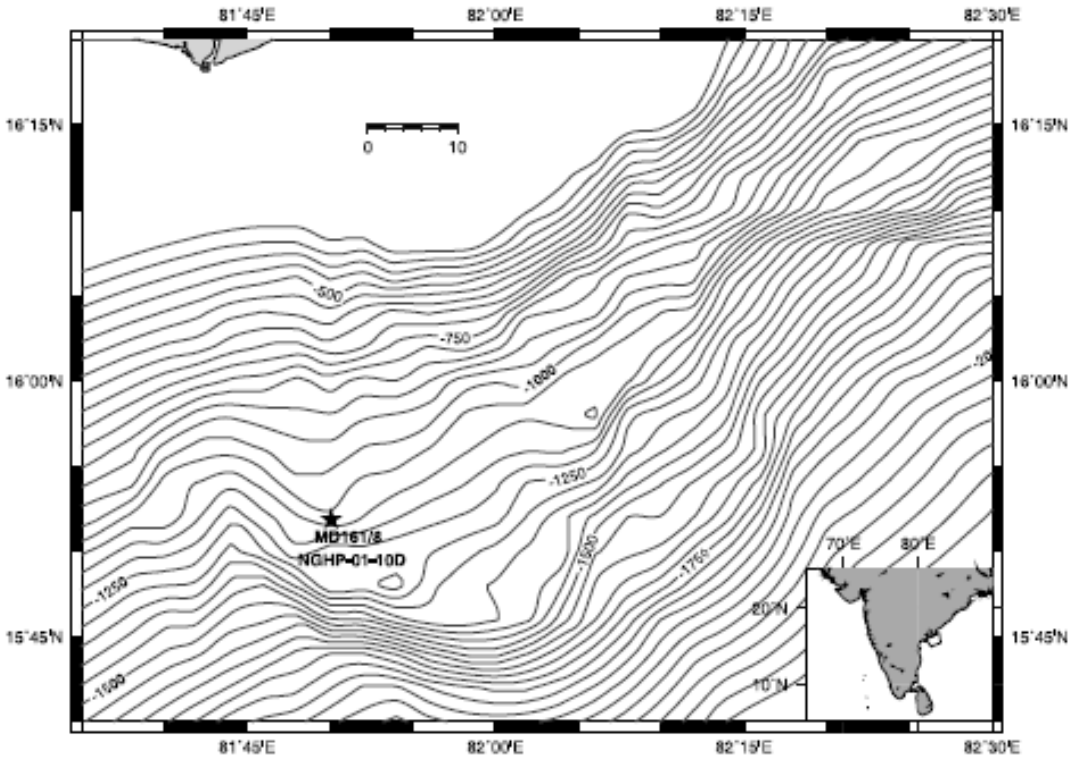

Figure1

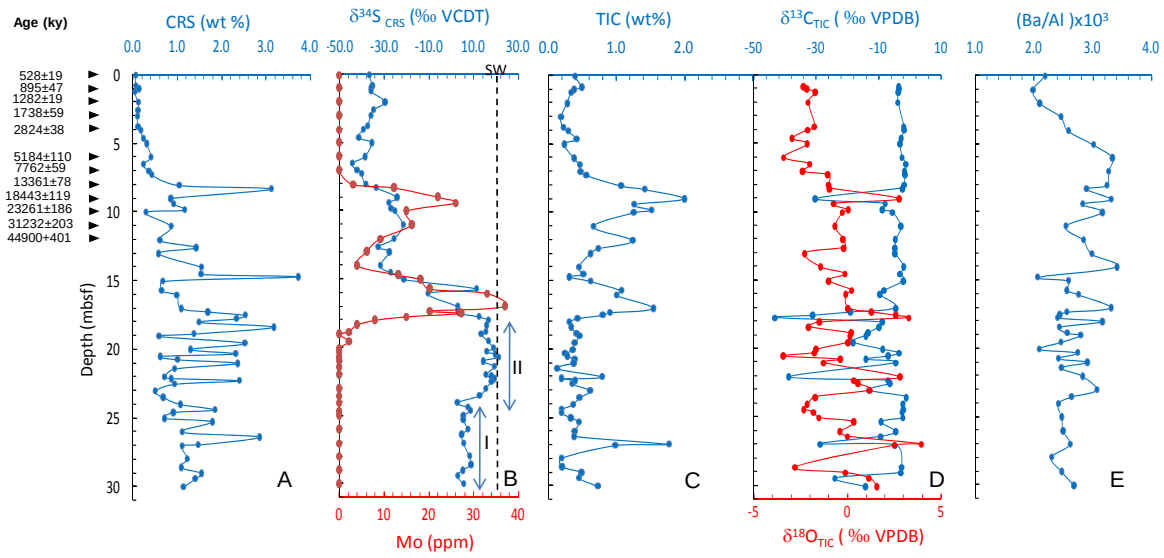

Figure 2

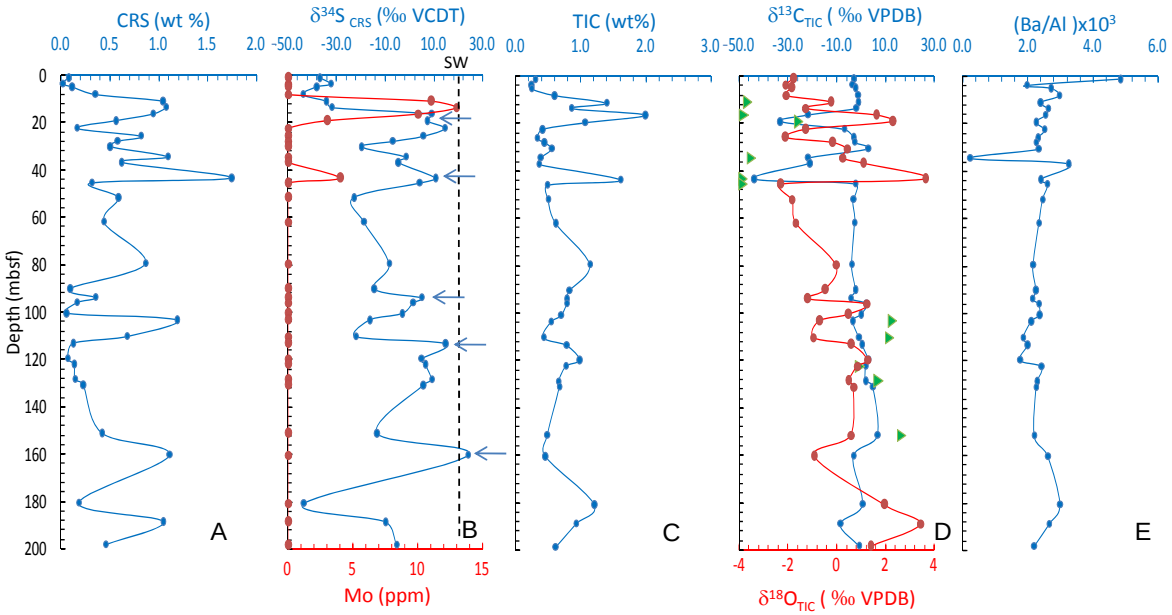

Figure3

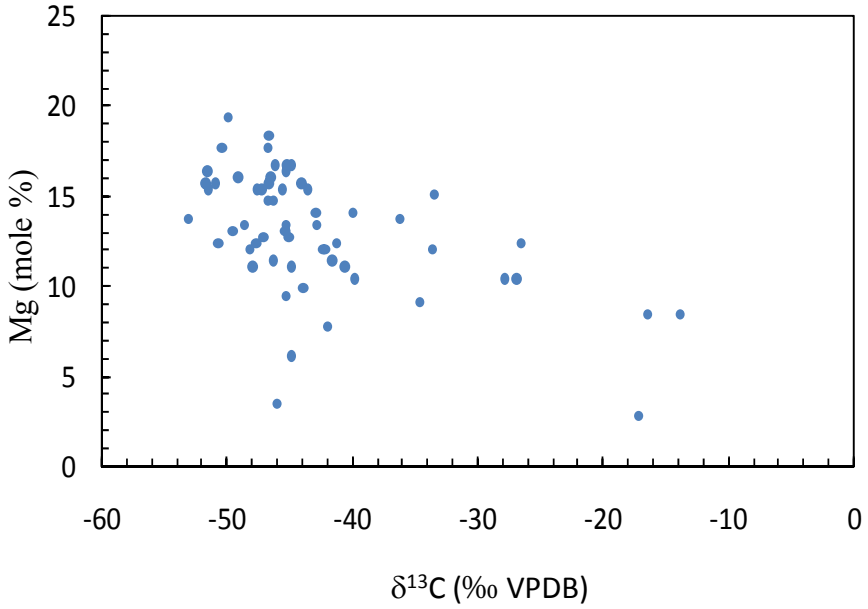

Figure 4

Table-1

Depth (m)	CRS (wt %)	$\delta^{34}S_{CRS}$ (‰ VCDT)	TIC (wt %)	$\delta^{13}C_{TIC}$ (‰ VPDB)	$\delta^{18}O_{TIC}$ (‰ VPDB)	TOC (wt %)	Ba (wt %)	Al (wt %)	Ba/Al	Mo (ppm)
0.05	0.06	-36.7	0.4	nm	nm	1.2	0.017	7.8	0.002	< 2
0.86	0.05	-35.4	0.5	-3.5	-2.3	1.0	nm	8.1	nm	nm
1.05	0.12	-36.0	0.4	-3.4	-2.1	1.2	0.017	8.6	0.002	< 2
1.28	0.04	-35.9	0.3	-3.6	-1.7	1.4	nm	8.2	nm	nm
2.05	0.11	-29.7	0.3	-3.8	-2.1	1.5	0.018	8.7	0.002	< 2
2.61	0.10	-35.0	nm	nm	nm	nm	nm	8.1	nm	nm
3.05	0.09	-36.1	0.2	nm	nm	1.6	0.021	8.4	0.002	< 2
3.81	0.10	-37.4	0.2	-1.9	-1.7	1.9	nm	9.0	nm	nm
4.05	0.17	-39.3	0.3	-1.7	-2.1	1.7	0.024	9.1	0.003	< 2
4.64	0.23	-41.5	0.4	-2.7	-2.9	1.6	nm	8.3	nm	nm
5.05	0.30	-35.7	0.2	-3.1	-2.1	1.9	0.026	8.6	0.003	< 2
6.05	0.40	-38.7	0.4	-2.5	-3.4	1.9	0.028	8.4	0.003	< 2
6.54	0.22	-44.4	0.5	-1.2	-2.0	2.0	nm	8.5	nm	nm
7.05	0.35	-42.2	0.5	-1.6	-2.4	1.6	0.028	8.6	0.003	< 2
7.32	0.41	-40.2	0.6	-1.5	-1.0	1.7	nm	8.6	nm	nm
8.05	1.03	-38.3	1.1	-1.7	-1.0	1.7	0.026	7.9	0.003	3
8.32	3.10	-33.6	1.4	-2.3	-0.9	1.6	0.021	7.3	0.003	12
9.05	0.84	-24.5	2.0	-30.3	2.8	1.2	0.023	7.0	0.003	22
9.42	0.90	-27.9	1.3	-7.8	-0.7	1.4	0.020	7.0	0.003	26
9.86	1.16	-27.2	1.5	-8.7	0.1	1.4	nm	7.3	nm	nm
10.05	0.28	-25.3	1.2	-5.5	-0.2	1.4	0.022	7.0	0.003	15
11.05	0.85	-21.7	0.7	-2.9	-0.6	1.4	0.020	8.0	0.003	16
12.05	0.59	-25.7	1.2	-4.6	-0.2	1.6	0.022	7.7	0.003	9
12.64	1.41	-32.8	0.7	-4.8	-0.2	2.1	nm	8.0	nm	nm
13.05	0.56	-27.8	0.6	-4.7	-2.3	1.8	0.024	8.0	0.003	6
14.05	1.53	-31.8	0.4	-1.9	-1.4	1.6	0.027	7.9	0.003	4
14.54	1.53	-27.3	0.5	-3.2	-0.1	1.2	nm	7.5	nm	nm
14.76	3.72	-23.8	0.3	nm	nm	1.5	0.017	8.2	0.002	13
15.05	0.66	-21.4	0.6	-2.0	-1.0	1.7	0.023	8.9	0.003	18
15.75	0.63	11.1	1.1	-8.1	0.2	2.1	0.019	7.6	0.003	20
16.05	0.98	-10.5	1.0	-9.5	-0.1	1.7	0.021	7.7	0.003	33
17.05	1.07	2.8	1.5	-4.5	0.1	1.3	0.028	8.4	0.003	37
17.32	1.67	2.6	0.9	-19.0	1.3	1.4	0.022	8.5	0.003	20
17.54	2.51	3.1	0.8	-31.0	2.6	1.3	0.021	8.6	0.002	27
17.76	2.32	12.2	0.4	-43.0	3.3	1.4	0.020	8.1	0.002	15
18.05	1.48	16.4	0.3	-8.7	-1.5	1.5	0.029	9.1	0.003	8
18.42	3.17	15.5	0.3	-9.8	-2.1	1.7	0.021	8.6	0.002	4
18.86	1.37	15.2	0.4	-13.4	0.2	1.5	0.021	8.1	0.003	2
19.05	0.57	13.1	0.5	-14.0	0.2	1.4	0.024	8.5	0.003	< 2

19.54	2.51	16.4	0.4	-18.2	0.1	1.4	0.020	8.2	0.002	2
20.05	1.29	18.6	0.4	-8.6	-1.7	1.0	0.016	7.8	0.002	< 2
20.32	2.30	15.6	0.2	-3.5	-1.8	1.5	0.022	7.9	0.003	< 2
20.54	0.61	19.3	0.3	-6.9	-3.4	1.4	nm	8.5	nm	nm
20.76	0.99	21.0	0.4	-14.0	-0.4	1.4	0.020	8.1	0.002	< 2
21.05	2.35	14.0	0.4	-4.5	-1.2	1.4	0.024	8.4	0.003	< 2
21.42	0.93	18.9	0.1	nm	nm	1.5	0.020	8.3	0.002	< 2
22.05	0.70	15.1	0.8	-38.7	2.8	1.4	0.025	8.8	0.003	< 2
22.16	0.85	17.7	0.2	nm	nm	1.4	nm	8.5	nm	nm
22.32	2.39	18.9	0.4	-6.8	0.4	1.3	nm	8.9	nm	nm
22.54	0.92	17.7	0.3	-6.3	0.6	1.6	nm	8.6	nm	nm
23.05	0.49	15.1	0.6	-13.0	1.2	1.4	0.025	8.0	0.003	< 2
23.54	0.67	12.4	0.5	-1.1	-1.7	1.5	0.021	8.1	0.003	< 2
24.05	1.05	2.6	0.4	-2.1	-2.1	1.8	0.021	8.9	0.002	< 2
24.42	1.84	7.3	0.2	-2.0	-2.3	1.8	nm	8.2	nm	nm
24.64	0.90	8.4	0.2	-2.4	-1.8	1.6	0.018	nm	nm	< 2
25.05	0.70	5.1	0.3	-2.2	-1.5	1.8	0.022	8.8	0.002	< 2
25.32	1.78	5.2	0.4	-9.1	0.3	2.0	nm	8.2	nm	nm
26.05	1.10	7.2	0.4	-4.5	-0.4	1.9	0.023	9.0	0.002	< 2
26.42	2.84	4.4	0.4	-9.2	0.0	2.0	nm	8.6	nm	nm
26.96	1.46	nm	1.8	-28.6	4.0	1.7	nm	7.2	nm	nm
27.05	1.10	5.4	1.0	-4.7	2.5	1.8	0.022	8.6	0.003	< 2
27.97	1.22	8.0	0.2	nm	nm	1.9	0.019	8.2	0.002	< 2
28.64	1.07	8.6	0.2	-2.6	-2.8	1.9	nm	8.2	nm	nm
29.05	1.54	5.0	0.5	-2.8	-0.1	1.7	0.022	9.0	0.002	< 2
29.45	1.39	2.7	0.4	-23.9	1.2	1.9	nm	8.2	nm	nm
30.05	1.12	5.4	0.7	-14.1	1.6	1.8	0.022	8.2	0.003	< 2

nm: not measured

Table-2

Sample name	Depth (m)	CRS (wt %)	$\delta^{34}S_{CRS}$ (‰ VCDT)	TIC (wt %)	$\delta^{13}C_{TIC}$ (‰ VPDB)	$\delta^{18}O_{TIC}$ (‰ VPDB)	TOC (wt %)	Ba (wt %)	Al (wt %)	Ba/Al	Mo (ppm)
1H1	1.4	0.08	-36.8	0.3	-3.0	-1.8	1.3	0.040	8.4	0.005	< 2
1H3	3.8	0.01	-32.3	0.2	-3.7	-2.1	1.4	0.018	9.1	0.002	< 2
2H1	5.2	0.11	-38.2	0.2	-2.4	-1.9	1.8	0.024	8.7	0.003	< 2
2H3	8.2	0.35	-43.8	0.6	-1.4	-2.1	2.0	0.027	9.1	0.003	< 2
2H5	11.2	1.04	-34.3	1.4	-1.2	-0.2	1.6	0.019	8.1	0.002	11
2H7	13.6	1.08	-31.9	0.9	-2.2	-1.3	1.9	0.022	8.4	0.003	13
3H2	16.5	0.94	8.9	2.0	-21.9	1.6	1.2	0.021	8.2	0.003	10
3H4	19.5	0.56	7.1	1.1	-33.3	2.3	1.3	0.020	9.1	0.002	3
3H6	22.5	0.16	14.3	0.4	-6.9	-1.3	1.4	0.022	8.7	0.003	< 2
4H2	26.0	0.82	5.4	0.3	-3.1	-2.1	1.9	0.020	8.5	0.002	< 2
4H4	28.0	0.57	-7.0	0.4	-2.8	-0.2	2.1	0.020	8.7	0.002	< 2
4H6	30.6	0.50	-19.9	0.5	2.7	0.4	2.1	0.020	8.7	0.002	< 2
5X2	34.5	1.09	-1.7	0.4	-22.0	0.2	1.8	0.002	8.9	0.000	< 2
5X5	37.1	0.62	-4.8	0.4	-21.1	1.1	1.5	0.028	8.5	0.003	< 2
7X2	43.7	1.74	10.5	1.6	-43.9	3.7	1.7	0.018	7.5	0.002	4
7X5	45.7	0.31	4.0	0.5	-2.4	-2.3	1.9	0.022	8.6	0.003	< 2
8X2	52.0	0.58	-22.9	0.5	-3.4	-1.8	1.4	0.020	8.3	0.002	< 2
10X2	62.0	0.44	-18.8	0.6	-2.6	-1.7	1.5	0.020	8.7	0.002	< 2
13X1	79.5	0.86	-8.5	1.1	-4.0	-0.04	1.1	0.019	9.0	0.002	< 2
14X2	90.4	0.09	-14.7	0.8	-2.5	-0.5	0.6	0.018	7.9	0.002	< 2
14X5	94.0	0.35	4.8	0.8	-4.4	-1.2	0.5	0.017	8.2	0.002	< 2
14X6	96.0	0.17	1.3	0.8	2.0	1.2	1.3	0.019	8.3	0.002	< 2
16X2	100.8	0.05	-3.0	0.7	-0.1	0.4	1.1	0.019	8.3	0.002	< 2
16X5	103.5	1.19	-16.4	0.5	-3.6	-0.7	1.3	0.019	9.2	0.002	< 2
17X2	110.3	0.67	-22.0	0.4	-1.0	-0.9	1.2	0.016	8.7	0.002	< 2
17X5	113.5	0.12	14.6	0.8	0.4	0.6	1.2	0.016	8.0	0.002	< 2
18X2	119.7	0.07	4.8	1.0	3.0	1.2	1.0	0.014	8.1	0.002	< 2
18X4	122.3	0.13	6.4	0.8	1.9	0.8	1.1	0.018	7.5	0.002	< 2
20X2	128.7	0.14	9.0	0.7	1.8	0.5	1.3	0.018	8.1	0.002	< 2
20X4	131.1	0.22	5.5	0.7	4.6	0.7	1.4	0.017	7.7	0.002	< 2
23X4	151.4	0.42	-13.5	0.5	6.5	0.5	1.5	0.018	8.0	0.002	< 2
24X4	160.4	1.10	24.0	0.5	-3.2	-0.9	1.0	0.022	8.4	0.003	< 2
27X4	180.7	0.18	-43.5	1.2	0.4	1.9	1.2	0.026	8.8	0.003	< 2
28X3	188.8	1.05	-10.0	0.9	-8.6	3.4	1.9	0.023	8.8	0.003	< 2
29X3	198.4	0.46	-5.3	0.6	-0.8	1.4	1.6	0.019	8.5	0.002	< 2

nm : not measured